

An augmented finite element method for modeling arbitrary discontinuities in composite materials

Daosheng Ling · Qingda Yang · Brian Cox

Received: 2 January 2009 / Accepted: 8 April 2009 / Published online: 8 May 2009
© Springer Science+Business Media B.V. 2009

Abstract An augmented finite element method (“A-FEM”) is presented that is a variant of the method of Hansbo and Hansbo (Comput Methods Appl Mech Eng, 193: 3523–3540, 2004), which can fully account for arbitrary discontinuities that traverse the interior of elements. Like the method of Hansbo and Hansbo, the A-FEM preserves elemental locality, because element augmentation is implemented within single elements and involves nodal information from the modified element only. The A-FEM offers the additional convenience that the augmentation is implemented via separable mathematical elements that employ standard finite element nodal interpolation only. Thus, the formulation is fully compatible with standard commercial finite element packages and can be incorporated as a user element without access to the source code. Because possible discontinuities include both elastic heterogeneity and cracks, the A-FEM is ideally suited to modeling damage evolution in structural or biological materials with complex morphology. Elements of a multi-scale approach to analyzing damage

mechanisms in laminated or woven textile composites are used to validate the A-FEM and illustrate its possible uses. Key capabilities of the formulation include the use of meshes that need not conform to the surfaces of heterogeneities; the ability to apply the augmented element recursively, enabling modeling of multiple discontinuities arising on different, possibly intersecting surfaces within an element; and the ease with which cohesive zone models of nonlinear fracture can be incorporated.

Keywords Finite element method · Cohesive zone model · Discontinuity · A-FEM · Textile composite

1 Introduction

1.1 Multi-scale modeling challenges in heterogeneous materials

High-fidelity simulations of damage evolution are approaching realization for a number of material systems, thanks to significant advances in modeling methods and experimental imaging (Ashby 1992; Cox and Yang 2006; Cox et al. 2008). Nevertheless, significant challenges remain, many of which relate to the difficulty of developing practicable formulations for dealing with materials containing complex material heterogeneity. Heterogeneity poses special problems with the accurate prediction of local stress and strain fields, which can vary strongly with local material features;

D. Ling
MOE Key Lab of Soft Soils and Geo-environmental Engineering, Zhejiang University, Hangzhou, China

Q. Yang (✉)
Department of Mechanical and Aerospace Engineering,
University of Miami, Coral Gables, FL 33124, USA
e-mail: qdYang@miami.edu

B. Cox
Teledyne Scientific Co LLC, Thousand Oaks, CA 91360, USA

and with predicting cracks and localized damage bands, which can appear during damage evolution not only on the material boundaries, but also on other surfaces that cannot be specified *a priori*. In both structural composites and biological materials (bone, dental enamel, dentin, wood, etc.), the complications of heterogeneity are repeated at different scales, because the materials are morphologically hierarchical.

In this article, the challenge problem of multi-scale modeling of laminated and textile composites is used to demonstrate the power of a new finite element formulation, the Augmented Finite Element Method or A-FEM. Crucial features of the A-FEM include: the ability to represent material heterogeneity accurately with a mesh that does not conform to the bounding surfaces of heterogeneities; the ability to introduce cracks on any surface during the execution of a calculation according to current values of stress or strain fields, without *a priori* specification of the crack path; the ability to augment elements recursively, i.e., introduce multiple cracking over increasingly finer scales; and the easy use of cohesive zone fracture models, which allow treatment of a wide physical range of localized damage bands or cracks. The question of when it is better on physical grounds to describe a fracture process using nonlinear process zones rather than a point process at the crack tip (linear elastic fracture mechanics) is also addressed.

1.2 Modeling interacting mechanisms in composite materials

Of particular concern in modeling damage in composites, with either textile or conventional 2D architecture, is the difficulty of dealing with multiple damage mechanisms that have strong interactions in an accurate and computationally efficient scheme. A typical case is coupled matrix cracking and interlaminar delamination in a 2D laminate, which remains an unresolved challenge in composite materials despite decades of extensive research. Lack of efficient analytical and numerical tools to quantitatively assess the coupling among multiple cracking events in composites prior to final failure is the bottle-neck in resolving this difficult and long-lasting problem (Cox and Yang 2006). The problem is further complicated by the fact that the exact locations of most of the multi-mode cracking events, which include transverse tunneling in off-axis

plies, fiber/matrix shear splitting in aligned plies, fiber rupture under tension, microbuckling under compression, and interlaminar delamination, cannot be known *a priori*.

While interlaminar delamination in composites has been studied extensively in the literature using various fracture mechanics models (e.g., Shahwan and Waas 1997; Tay 2003; Yang and Cox 2005), the intra-ply damage modes (transverse cracking, shear splitting, and fiber rupture/microbuckling) have been studied mainly under the framework of continuum damage mechanics (CDM) (e.g., McCartney 2003; Chang et al. 1991 and Talreja 2006). Meso-scale averaging evoking assumed periodicity is typically used in CDM to obtain homogenized constitutive relations. Direct coupling of CDM-based in-plane damage modes with various fracture mechanics models for delamination has also been attempted by several research groups but with only limited success (e.g., Cox and Yang 2006; Van de Meer and Sluys 2008; Carpinteri and Ferro 2003). Several recent studies have revealed that the homogenization process in CDMs leads to loss of key information on multiple-damage coupling at the macroscopic scale and results in inaccurate prediction of crack paths (Van de Meer and Sluys 2008; Talreja 2006) and severe stress locking (Iarve and Mollenhauer 2005).

The inadequacy of CDM has led to the recent trend of pursuing explicit representations of all major matrix cracking events in composite structural models to achieve direct coupling (Iarve and Mollenhauer 2005; Gonzalez and Lorca 2006; Hallett and Wisnom 2006). These direct coupling analyses are enabled by two recent developments, viz., improved cohesive zone models (CZMs) for bulk and interface crack problems, and new finite element method (FEM) formulations for arbitrary crack initiation and extension such as the extended FEM (X-FEM) (Belytschko and Black 1999; Moes and Belytschko 2002).

Cohesive zone models (CZMs) have been widely used in composite fracture analysis, especially in delamination analyses (Shahwan and Waas 1997; Wisnom and Chang 2000; Carpinteri and Ferro 2003; Yang and Cox 2005; Cox and Yang 2006; Hallett and Wisnom 2006; Xie et al. 2006). However, the traditional CZM approach carries the major shortcoming that it requires the potential crack path to be known *a priori*, so that CZM elements can be directly implanted along the path. This greatly limits the application of CZM for problems with evolving arbitrary discontinuities.

1.3 The extended finite element method (X-FEM)

A promising solution to the CZM shortcoming is to integrate a CZM formulation into the framework of the X-FEM, because the X-FEM is particularly effective in dealing with moving arbitrary discontinuities. This combination was first reported by (Belytschko and Black 1999) and extended by (Moes et al. 1999). The need of remeshing when a crack advances is eliminated by introducing local enrichment to the cracked elements. The local enrichment procedure is based on the partition-of-unity finite element method (PUFEM) first proposed by (Melenk and Babuska 1996), and employs the known asymptotic displacement field for the non-linear crack tip regions and the generalized Heaviside function for the traction-free crack wake region. A variety of fracture problems of interest in engineering materials and structures have recently been modeled by these methods (Gravouil et al. 2002; Moes et al. 2002; Moes and Belytschko 2002; Wells et al. 2002; De Borst 2003; Remmers 2006).

The key feature in X-FEM formulation is the use of enrichment functions for cracked elements locally. This is achieved by enhancing the degrees of freedom (DoFs) of all the nodes employed by the elements with internal discontinuity. A general expression for the displacement field can be written as

$$\mathbf{u}(\mathbf{x}) = \sum_{i \in I} N_i(\mathbf{x}) \mathbf{d}_i + \sum_{j \in E} N_j(\mathbf{x}) \varphi(\mathbf{x}) \mathbf{a}_j \quad (1)$$

where $N_i(\mathbf{x})$ is the standard FE shape function at node i , \mathbf{d}_i are the nodal displacements, $\varphi(\mathbf{x})$ are the proper enrichment functions and \mathbf{a}_j the additional DoFs corresponding to the enrichment. The set I is the entire element node set and E ($E \subseteq I$) is the sub-set consisting of the enriched nodes. An important feature of the method is that since the shape functions $N_i(\mathbf{x})$ multiply the enrichment term, this term is also local, so the discrete equations will be sparse. A review of this promising method is given by Karihaloo and Xiao (2003).

Note that in Eq. 1, the first term is identical to the regular finite element nodal interpolation and it approximates the continuous part of the displacements. The second term represents the contribution to nodal displacements from the discontinuity and it is local to the enriched nodes only. If such an element is traversed by a traction-free crack, i.e., $\phi(\mathbf{x}) = H(\mathbf{x})$ with $H(\mathbf{x})$ being the Heaviside function (jump function), the degrees of freedom \mathbf{a}_j enable the method to vary the

amount of crack opening within the element. Through a novel manipulation of the jump function to form the “shift function”, Belytschko et al. (2001) were able to make such an element completely local and compatible with regular finite elements. For an element that encompasses a singular crack-tip, asymptotic displacement functions from fracture mechanics are needed as enrichment functions and the enrichment process leads to the loss of elemental locality in the sense that the blending elements, i.e., the uncracked elements that share the enriched nodes with the crack tip element, have to be treated simultaneously (Moes et al. 1999, 2002; Remmers 2006). Additional ambiguities for the blending elements can arise and need special treatment (Chessa et al. 2003; Fries and Belytschko 2006). For these reasons, it is difficult to integrate such an element into existing standard finite element programs.

1.4 The augmented finite element method (A-FEM)

It is, therefore, of great interest to develop a new finite element method that can deal with arbitrary internal discontinuities but maintain the essential FEM advantage of elemental locality, so that it can be readily integrated into existing standard FEM programs. A key response to this challenge is the recent work of Hansbo and Hansbo (2002, 2004), who proposed an interesting method for modeling arbitrary strong and weak discontinuities without the use of local enrichment functions. The discontinuities could be strong, i.e., crack-like discontinuities in the displacement field, or weak, i.e., discontinuities in the displacement gradient such as due to material heterogeneity. The method is an extension of Nitsche’s method and uses dual elements with standard shape functions (but truncated across a discontinuity) to account for the displacement fields in a physical domain traversed by a discontinuity. The formulation is different from X-FEM but it has been shown by Areias and Belytschko (2006) that they are equivalent—the basis functions in Hansbo and Hansbo’s element are simply a linear combination of the X-FEM basis functions. More recently, Steinmann and colleagues have coupled Hansbo and Hansbo’s method with CZMs to cope with arbitrary fracture problems in homogeneous, isotropic materials (Jager et al. 2008; Mergheim et al. 2007, 2005). The material heterogeneity issue, which is of paramount importance in

composite materials (whether laminated plies or textile), has yet to be addressed.

In this paper, we report an augmented finite element method (A-FEM) that can adequately describe arbitrary discontinuities but, like Hansbo and Hansbo's method, does not require introducing enrichment functions. It fully preserves elemental locality and hence can be made compatible with commercial FEM programs. This is enabled by the recognition that a physically cracked element (physical mesh) can be represented by two separable mathematical elements possessing standard finite element structure. The proposed formulation enables the use of standard finite element shape functions without any truncation across the discontinuity, which greatly facilitates the use of the augmented elements in conjunction with cohesive zone modes. Reciprocally, the influence of a cohesive zone (or nonlinear fracture process zone) on stress fields around a crack tip has an important role in determining the optimal numerical formulation and mesh choice; calculations are presented that demonstrate how the characteristic length of the cohesive zone controls the stress concentration at the crack tip for realistic cohesive laws. Further, the A-FEM allows for the explicit consideration of different material properties in different sub-element domains; thus, material heterogeneity, if it exists, is conveniently accounted for with a mesh that need not conform to the heterogeneity boundaries.

1.5 Scope of this paper

The paper is organized as follows: Sect. 2 presents the strong and weak forms of the A-FEM for nonlinear cohesive fracture mechanics. Section 3 introduces the formulation and mathematical proof of the equivalence of the proposed method to standard FEM. Numerical implementation of the augmented element will also be discussed in this section. In Sect. 4, the challenge problem of formulating a multi-scale model of a textile composite is addressed, using three numerical examples to demonstrate the validity and capability of the proposed method for key sub-problems of an eventual, integrated multi-scale model. This will be followed by a discussion section (Sect. 5) to highlight the benefits and potential applications, and the role of length scales implied by a cohesive zone in deciding whether X-FEM (point fracture process) or A-FEM (cohesive zone fracture model) is the physically appropriate

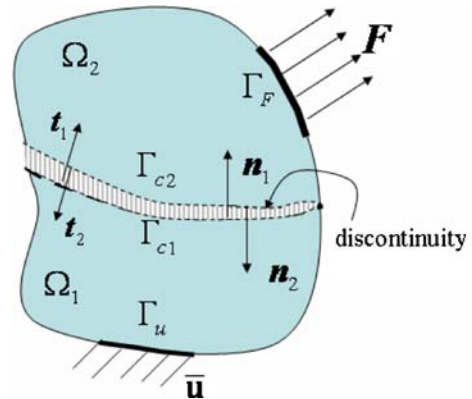


Fig. 1 Notation for a body with an arbitrary discontinuity

formulation. Finally, Sect. 6 will provide summaries and conclusions.

2 Problem statement

The mathematics underlying the A-FEM formulation has been published previously by Hansbo and Hansbo (2004). Notwithstanding, the present authors' formulation is detailed here, because it uses language that is more familiar to the composites modeling community.

2.1 Strong and weak form

Consider a discontinuous physical domain (DPD) Ω as shown in Fig. 1. The domain is composed of two sub-domains of same or different materials, i.e., $\Omega = \Omega_1 \cup \Omega_2$. The two domains are connected by a discontinuity which could be a cohesive crack or a material boundary, $\Gamma_c = \Gamma_{c1} \cup \Gamma_{c2}$.¹ The prescribed tractions F are imposed on boundary Γ_F and the prescribed displacements \bar{u} on boundary Γ_u . The stress field inside the domain, σ , is related to the external loading F and the tractions t_1 and t_2 along the discontinuity through the equilibrium equations:

$$\begin{aligned} \nabla \cdot \sigma &= 0 & (\text{in } \Omega = (\Omega_1 \cup \Omega_2) \setminus \Gamma_c) \\ \sigma \cdot n &= F & (\text{on } \Gamma_F) \\ u &= \bar{u} & (\text{on } \Gamma_u) \\ t_1 &= \sigma \cdot n_1 = t & (\text{on } \Gamma_{c1}) \\ t_2 &= -\sigma \cdot n_2 = -t & (\text{on } \Gamma_{c2}) \end{aligned} \quad (2)$$

¹ For a weak discontinuity $\Gamma_{c1} = \Gamma_{c2}$ while for a strong discontinuity Γ_{c1} and Γ_{c2} are separated.

The last two equations in (2) come from the stress continuity across the discontinuity boundary. The traction, \mathbf{t} , is a function of the relative displacements, \mathbf{w} , between Γ_{c1} and Γ_{c2} , i.e.,

$$\begin{aligned} \mathbf{t} &= \mathbf{t}(\mathbf{w}) \text{ (on } \Gamma_c) \\ \mathbf{w} &= \mathbf{u}_2 - \mathbf{u}_1 \text{ (on } \Gamma_c) \end{aligned} \quad (3)$$

where \mathbf{u}_1 and \mathbf{u}_2 are the displacement fields in Ω_1 and Ω_2 , respectively. Equation (3) serves as the constitutive law and kinematic equation of the discontinuity. In this study, we use a cohesive zone model to describe the constitutive law of a discontinuity, which will be introduced shortly in Sect. 2.2.

The domain surrounding the discontinuity is assumed to be elastic. We further assume small strains and displacement condition. Thus, the constitutive law and geometric equation for the domain can be written as

$$\begin{aligned} \boldsymbol{\sigma} &= \mathbf{C} : \boldsymbol{\epsilon} \text{ (in } \Omega \setminus \Gamma_c) \\ \boldsymbol{\epsilon} &= \boldsymbol{\epsilon}(\mathbf{u}) = [\nabla \mathbf{u} + (\nabla \mathbf{u})^T] / 2 \text{ (in } \Omega \setminus \Gamma_c) \end{aligned} \quad (4)$$

with \mathbf{C} being the material stiffness tensor. The superscript $(\cdot)^T$ denotes transposition.

The above strong form of the problem can be converted into a weak form using the principle of virtual work. The displacement \mathbf{u} must be one of the set of kinematically admissible displacements, \mathbf{U}

$$\mathbf{u} \in \mathbf{U} = \{\mathbf{v} \in \mathbf{V} : \mathbf{v} = \mathbf{0} \text{ on } \Gamma_u\}. \quad (5)$$

The weak form can then be written as (Moes and Belytschko 2002)

$$\begin{aligned} \int_{\Omega} \boldsymbol{\sigma} : \boldsymbol{\epsilon}(\mathbf{v}) \, d\Omega + \int_{\Gamma_c} \mathbf{t} \cdot \mathbf{w}(\mathbf{v}) \, d\Gamma &= \int_{\Gamma_F} \mathbf{F} \cdot \mathbf{v} \, d\Gamma \\ \forall \mathbf{v} \in \mathbf{U} \end{aligned} \quad (6)$$

2.2 Constitutive law for a CZM of polymer composite fracture

In the following numerical studies, we will use the mixed-mode cohesive law developed by Yang and Thouless (2001) for each of the different fracture mechanisms addressed. This generic cohesive law utilizes separate traction separations for opening (mode-I) and shear (mode-II) cracking, i.e.,

$$\begin{aligned} t_n &= t_n(w_n) = \begin{cases} \hat{\sigma} \cdot (w_n/w_{n1}) & (w_n \leq w_{n1}) \\ \hat{\sigma} & (w_{n1} < w_n \leq w_{n2}) \\ \hat{\sigma} \cdot \frac{(w_{nc}-w_n)}{(w_{nc}-w_{n2})} & (w_{n2} < w_n \leq w_{nc}) \\ 0 & (w_n > w_{nc}) \end{cases} \\ t_s &= t_s(w_s) = \begin{cases} \hat{\tau} \cdot (w_s/w_{s1}) & (|w_s| \leq w_{s1}) \\ \text{sgn}(w_s) \cdot \hat{\tau} & (w_{s1} < |w_s| \leq w_{s2}) \\ \text{sgn}(w_s) \cdot \hat{\tau} \cdot \frac{(w_{sc}-|w_s|)}{(w_{sc}-w_{s2})} & (w_{s2} < |w_s| \leq w_{sc}) \\ 0 & (|w_s| > w_{sc}) \end{cases} \end{aligned} \quad (7)$$

where $\text{sgn}(\cdot)$ is a sign function, and $|\cdot|$ denotes absolute value; t_n and t_s are normal and tangential tractions along the cohesive crack; w_n and w_s are normal and tangential displacement jumps; w_{nc} and w_{sc} are critical normal and tangential displacement jumps under pure modes beyond which the cohesive stresses become zero, indicating complete fracture; and $\hat{\sigma}$ and $\hat{\tau}$ are peak stresses for mode-I and mode-II fracture, respectively. The two displacements of each mode, w_{n1} and w_{n2} for mode-I, and w_{s1} and w_{s2} for mode-II, dictate the shapes of the cohesive laws but they are in general of secondary importance (Yang et al. 1999; Tvergaard and Hutchinson 1996). The cohesive laws are illustrated in Fig. 2.

A mixed-mode cohesive model can be constructed by recognizing that the total traction-separation work absorbed during fracture \mathcal{G} can be separated into the opening (mode-I) and shear (mode-II) components, \mathcal{G}_I and \mathcal{G}_{II} , so that,

$$\mathcal{G} = \mathcal{G}_I + \mathcal{G}_{II} \quad (8)$$

The two separate components can be calculated by integration of the mode-I and mode-II traction-separation curves (Fig. 2):

$$\begin{aligned} \mathcal{G}_I(w_n) &= \int_0^{w_n} t_n(w) dw \\ \mathcal{G}_{II}(w_s) &= \int_0^{w_s} t_s(w) dw, \end{aligned} \quad (9)$$

Note that w_n and w_s are not independent parameters; they evolve together as a natural result of the interplay between the deformation of two joined domains and the details of the two traction-separation laws. A failure criterion is required to determine the critical values of the two components of \mathcal{G} , $\mathcal{G}_I(w_n^*)$ and $\mathcal{G}_{II}(w_s^*)$ (shaded areas in Fig. 2), at which complete fracture of the cohesive zone occurs. The criterion used in this study is a simple one (Wang and Suo 1990):

$$\mathcal{G}_I(w_n^*) / \Gamma_I + \mathcal{G}_{II}(w_s^*) / \Gamma_{II} = 1, \quad (10)$$

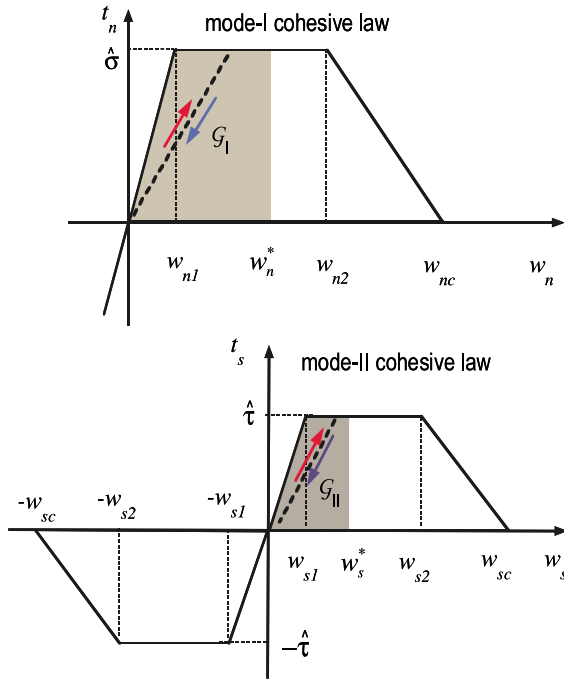


Fig. 2 Mixed-mode cohesive zone model used in this study

where Γ_I and Γ_{II} are the *total* areas under the pure opening and pure shear traction-separation laws. They are the mode-I and mode-II fracture toughnesses in LEFM.

A more detailed account of this mixed-mode cohesive zone model can be found in [Yang and Thouless \(2001\)](#). The major advantage of this cohesive law is that there is no need to specify the mode mixture a priori. The mode mixture and the mixed-mode toughness evolve as numerical outcomes of the local equilibrium of stresses.

3 The augmented finite element formulation and implementation

3.1 Element formulation

In this section, we shall describe how to use two standard finite elements to fully represent a physical element with weak or strong discontinuities. Without the loss of generality, we choose the 4-node quadratic plane element to illustrate the augmented finite element scheme. The physical element (1-2-3-4) is severed by

a cohesive crack where the tractions are continuous but displacements are not as shown in [Fig. 3](#).²

Before we proceed to the numerical formulation, we first briefly review how standard FEM and X-FEM would treat the problem, in order to appreciate the difference among the proposed method, the X-FEM, and standard FEM. Traditional FEM cannot deal with the displacement discontinuity without knowing the crack path a priori. If the crack path is known, traditional FEM would have to use two elements, e.g., 1-2-6-5 (standard element 1—SE 1) and 8-7-3-4 (standard element 2—SE 2), in addition to a cohesive element 5-6-8-7 to fully describe the mechanical responses. Using the standard shape function interpolation, the displacement fields, \mathbf{u}_α , in the two SEs can be written as,

$$\mathbf{u}_\alpha = \mathbf{N}_\alpha \cdot \mathbf{d}_\alpha; \quad (11)$$

where \mathbf{d}_α is the nodal displacement array of standard element α ($\alpha = 1$ and 2), and $\mathbf{N}_\alpha(\mathbf{x})$ is the bi-linear interpolation matrix of the element. Under the assumption of small deformation, the strain can be obtained as

$$\epsilon_\alpha = (\mathbf{L}^T \mathbf{N}_\alpha) \cdot \mathbf{d}_\alpha = \mathbf{B}_\alpha \cdot \mathbf{d}_\alpha; \quad (12)$$

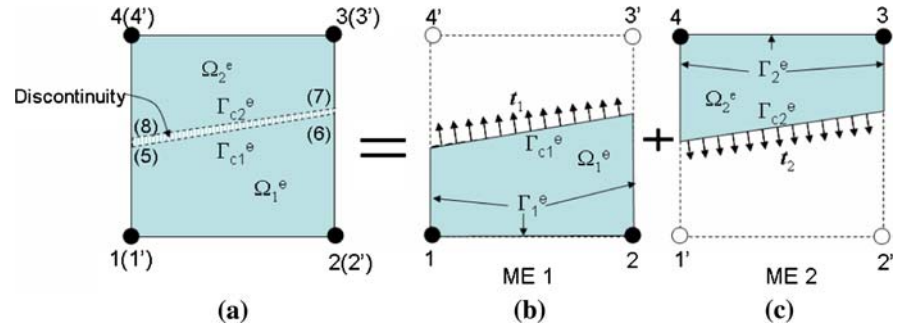
where \mathbf{L} is the differentiation operator, i.e., $\mathbf{L} = \begin{bmatrix} \partial/\partial x & 0 & \partial/\partial y \\ 0 & \partial/\partial y & \partial/\partial x \end{bmatrix}$. Substituting Eqs. 11 and 12 into Eq. 6 and using the principle of virtual work, one obtains the weak form of the equilibrium equation for standard elements

$$\mathbf{K}_\alpha \cdot \mathbf{d}_\alpha = \bar{\mathbf{f}}_\alpha + \mathbf{f}_\alpha \quad (13)$$

where $\mathbf{K}_\alpha = \int_{\Omega_\alpha^e} \mathbf{B}_\alpha^T \cdot \mathbf{D}_\alpha \cdot \mathbf{B}_\alpha d\Omega$ is the elemental stiffness matrix of standard element α , $\bar{\mathbf{f}}_\alpha = \int_{\Gamma_\alpha^e} \mathbf{N}_\alpha^T \cdot \mathbf{F}_\alpha d\Gamma$ and $\mathbf{f}_\alpha = \int_{\Gamma_{ca}^e} \mathbf{N}_\alpha^T \cdot \mathbf{t}_\alpha d\Gamma$ are the nodal force arrays contributed from the boundary tractions and from the internal tractions due to discontinuity, respectively. \mathbf{D}_α is the material stiffness matrix. Note that for this standard finite element method, the SEs are coupled by the cohesive tractions, and the jump in displacement fields across the discontinuity is accounted for by the additional cohesive zone element ([Yang et al. 1999](#); [Yang and Thouless 2001](#); [Camanho et al. 2003](#)). Therefore,

² Here, we take a common approach by assuming (1) during crack growth, a crack tip always resides at an element boundary during its propagation ([Remmers 2006](#); [De Borst 2003](#)), and (2) the existence of a cohesive zone eliminates the crack-tip singularity ([Moes et al. 2002](#); [Yang et al. 2005](#)). See detailed discussion in Sect. 5.

Fig. 3 Illustration of the current method of representing with different active material domains discontinuous physical domain (a) by two mathematical elements (b and c) with different active material domains



the displacements at corner nodes 1–4 are total displacements, that is, they include contributions from elemental straining and the displacement jump across the discontinuity.

X-FEM can account for the discontinuous displacement field using a single element (1-2-3-4). This is done by introducing additional degree of freedoms (DoFs) associated with the enrichment functions (asymptotic solutions of a cohesive or singular crack-tip). The local enrichment is done on a nodal-based procedure: a node is enriched only after its entire support (the domain that covers all the elements that share the node) is completely cut. Moreover, if the cohesive opening is large enough that a traction free crack has formed, the asymptotic basis functions will have to be switched to the general Heaviside function (Moes and Belytschko 2002).

The augmented FEM (A-FEM) introduced in this paper will allow us to account for discontinuity within a single physical element that uses standard FE nodal shape functions only. We first demonstrate that the discontinuous displacement field in $\Omega^e = \Omega_1^e \cup \Omega_2^e$ can be fully described by superposition of two standard elements (which we shall subsequently refer to as “mathematical elements”—MEs) that utilize only the standard shape functions. This can be done through a mapping procedure that extrapolates the displacement fields of the two physical domains, Ω_1^e and Ω_2^e , into the two mathematical elements as shown in Fig. 3. Both MEs have the identical geometry of the discontinuous physical element (Ω^e) and use standard shape functions for elemental displacement field interpolation, but with different material allocation. In ME1, which represents the physical response of Ω_1^e , the active material domain for stiffness and nodal force integration has the identical geometry of Ω_1^e , while the rest of the ME1 does not contribute to the stiffness of the element. Two additional nodes 3' and 4' are introduced to facilitate the elemental displacement interpolation and they share

the same geometrical locations with the corresponding physical nodes (3 and 4). Similarly, ME2 represents the physics response of Ω_2^e with two added nodes 1' and 2'. We shall subsequently name these added nodes as “ghost nodes”. It is emphasized here that these ghost nodes are merely introduced to facilitate the elemental displacement interpolation using standard shape functions. They are not shared by any neighboring elements other than those elements traversed by the same discontinuity.

Within the MEs, standard nodal shape functions are used to interpolate the displacement field, \mathbf{u}'_α ,

$$\mathbf{u}'_\alpha = \mathbf{N}'_\alpha \cdot \mathbf{d}'_\alpha \quad (14)$$

where \mathbf{d}'_α is the nodal displacement array and $\mathbf{N}'_\alpha(\mathbf{x})$ is the bi-linear interpolation matrix of ME α ($\alpha = 1$ and 2). Note that \mathbf{N}'_α in Eq. 14 is different from \mathbf{N}_α in Eq. 11 because the ME has a different geometry with its corresponding physical domain. With Eq. 14, the equilibrium equations for the MEs can be written as

$$\mathbf{K}'_\alpha \cdot \mathbf{d}'_\alpha = \bar{\mathbf{f}}'_\alpha + \mathbf{f}'_\alpha, \quad (15)$$

where

$$\begin{aligned} \mathbf{K}'_\alpha &= \int_{\Omega_\alpha^e} \mathbf{B}_\alpha^T \cdot \mathbf{D}_\alpha \cdot \mathbf{B}_\alpha d\Omega, \\ \mathbf{f}'_\alpha &= \int_{\Gamma_{c\alpha}^e} \mathbf{N}_\alpha^T \cdot \mathbf{t}_\alpha d\Gamma \\ \bar{\mathbf{f}}'_{c\alpha} &= \int_{\Gamma_{c\alpha}^e} \mathbf{N}_\alpha^T \cdot \mathbf{F}_\alpha d\Gamma. \end{aligned} \quad (16)$$

Note that the stiffness integration (first equation of Eq. 16) within a mathematical element is performed on the active material domain (i.e., Ω_1^e for ME1 or Ω_2^e for ME2), rather than on the entire elemental domain $\Omega^e (= \Omega_1^e \cup \Omega_2^e)$. This is important because it offers extra flexibility in handling material heterogeneity across the

discontinuity: by simply using different \mathbf{D}_α during the integration will achieve the purpose.

In the following, we shall briefly prove the equivalence of Eq. 15, the equilibrium equation of mathematical elements, and Eq. 13, the equilibrium equation of the standard elements. First, we note that there always exists a mapping matrix, \mathbf{T}_α , which correlates the nodal displacement array of a ME to the corresponding SE. That is,

$$\mathbf{d}_\alpha = \mathbf{T}_\alpha \cdot \mathbf{d}'_\alpha \quad (17)$$

For example, the mapping matrix \mathbf{T}_1 , which correlates the nodal displacement of SE1 (1-2-6-5) to ME 1 (1-2-3'-4'), can be constructed as

$$\mathbf{T}_1 = \begin{bmatrix} 1 & 0 & 0 & 0 & 0 & 0 & 0 & 0 \\ 0 & 1 & 0 & 0 & 0 & 0 & 0 & 0 \\ 0 & 0 & 1 & 0 & 0 & 0 & 0 & 0 \\ 0 & 0 & 0 & 1 & 0 & 0 & 0 & 0 \\ 0 & 0 & N'_2(6) & 0 & N'_{3'}(6) & 0 & 0 & 0 \\ 0 & 0 & 0 & N'_2(6) & 0 & N'_{3'}(6) & 0 & 0 \\ N'_1(5) & 0 & 0 & 0 & 0 & 0 & N'_{4'}(5) & 0 \\ 0 & N'_1(5) & 0 & 0 & 0 & 0 & 0 & N'_{4'}(5) \end{bmatrix} \quad (18)$$

In Eq. 18, $N'_i(j)$ denotes the value of shape function of node i in the ME, evaluated at the geometrical location of the physical point j (j is in general not an element corner node in a ME). In deriving Eq. 18, $N'_2(5) = N'_{3'}(5) = N'_1(6) = N'_{4'}(6) = 0$ were used. Note all the matrix elements in matrix \mathbf{T}_1 are constants. Substituting Eq. 18 into Eq. 11 gives,

$$\mathbf{u}_1 = \mathbf{N}_1 \cdot \mathbf{T}_1 \cdot \mathbf{d}'_1 = \bar{\mathbf{N}}_1 \cdot \mathbf{d}'_1; \quad (19)$$

where $\bar{\mathbf{N}}_1 = \begin{bmatrix} \bar{N}_1 & 0 & \bar{N}_2 & 0 & \bar{N}_{3'} & 0 & \bar{N}_{4'} & 0 \\ 0 & \bar{N}_1 & 0 & \bar{N}_2 & 0 & \bar{N}_{3'} & 0 & \bar{N}_{4'} \end{bmatrix}$, and

$$\begin{aligned} \bar{N}_1 &= N_1 + N'_1(5) N_5; & \bar{N}_2 &= N_2 + N'_2(6) N_6; \\ \bar{N}_{3'} &= N'_{3'}(6) N_6; & \bar{N}_{4'} &= N'_{4'}(5) N_5 \end{aligned}$$

It can be easily verified that all the \bar{N}_i ($i = 1, 2, 3', 4'$) strictly satisfy all the required properties for standard FE shape functions. Since the same bi-linear interpolation is applied to both the SE and ME, it follows from the uniqueness of nodal shape functions interpolation (with a fixed order) that $\bar{N}_i = N'_i$ ($i = 1, 2, 3', 4'$). Then Eq. 19 leads to the conclusion that $\mathbf{u}_1 = \mathbf{N}'_1 \cdot \mathbf{d}'_1$ (in Ω^e_1). A similar mapping matrix, \mathbf{T}_2 , can be constructed for ME2 and it can be similarly proved that

$\mathbf{u}_2 = \mathbf{N}'_2 \cdot \mathbf{d}'_2$ (in Ω^e_2). Thus, we have proved that

$$\begin{aligned} \mathbf{u}_\alpha &= \mathbf{N}'_\alpha \cdot \mathbf{d}'_\alpha \quad (\text{in } \Omega^e_\alpha), \\ \mathbf{N}'_\alpha &= \mathbf{N}_\alpha \cdot \mathbf{T}_\alpha \end{aligned} \quad (20)$$

Finally, by substituting Eqs. 17 and 20 into the equilibrium equation of Eq. 15 and making use of the fact that \mathbf{T}_α is matrix of constants, the equivalence of the equilibrium equations on the standard elements and their corresponding mathematical elements can be easily verified.

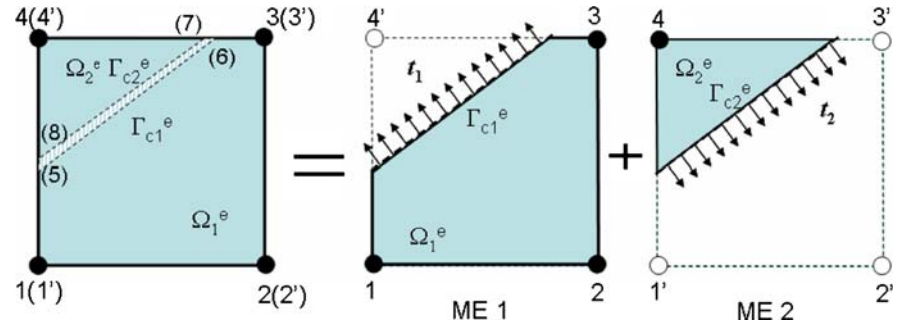
Thus, we have proved that the mechanical response of the discontinuous physical domain (1-2-3-4) can be fully represented by two MEs with the same geometry but different stiffness integration domains (SIDs). The

fact that the geometry of both MEs is identical to that of the discontinuous physical domain further allows us to re-cast Eqs. 14–16 into a single augmented element with double nodes for each corner, which will be detailed in Sect. 3.2.

In the more general case that the physical domain Ω^e is severed into two parts comprising a triangle and a pentagon, the two MEs can be defined as shown in Fig. 4. In this case, sub-domain integration on the MEs is needed to obtain their stiffnesses.

Equation (20) states that the displacement field of a SE can be directly obtained from standard elemental interpolation of the related ME within the active domain. This is the key advantage of the current method and it offers several immediate benefits. The first is that it guarantees that the displacements of all physical nodes (1–4 in Fig. 3) are total displacements, i.e., they include both continuous displacements and discontinuous displacements. This can be seen from the fact that, in the current formulation, the physical nodes are always associated with the active domain in a ME. Therefore, the nodal displacements of the physical nodes should be the same as the displacements that

Fig. 4 Mathematical element definition if a physical domain is separated by a discontinuity into a triangular and a pentagon sub-domain



would be obtained from a traditional FEM and CZM calculation, which, as discussed above, are total displacements.

The second important benefit is that the method is very flexible in treating discontinuities with a variety of constitutive laws. Note that in the current formulation, the jump in displacements across the discontinuous boundary can be obtained through nodal interpolation of the two MEs at the discontinuous boundary, i.e.,

$$\mathbf{w} = \mathbf{N}'_2 (\Gamma_{c2}^e) \cdot \mathbf{d}'_2 - \mathbf{N}'_1 (\Gamma_{c1}^e) \cdot \mathbf{d}'_1 \quad (21)$$

Thus, a weak discontinuity can be achieved by simply enforcing $\mathbf{d}'_2 = \mathbf{d}'_1$ (i.e., $\mathbf{w} = 0$) and a strong discontinuity can be obtained by introducing a proper constitutive description such as the cohesive law $\mathbf{t} = \mathbf{t}(\mathbf{w})$ discussed in Sect. 2.2. Therefore, the current formulation can account for the entire spectrum of discontinuities ranging from rigid bonding ($\mathbf{w} = 0$), to non-linear cohesive fracture ($\mathbf{t} = \mathbf{t}(\mathbf{w})$), and to a traction free crack ($\mathbf{t}(\mathbf{w}) \equiv 0$, i.e., \mathbf{d}'_2 and \mathbf{d}'_1 are independent). This generality was foreseen by Hansbo and Hansbo (2002, 2004), although they did not demonstrate it in detail.

3.2 Numerical implementation

Based on the above formulation, designing an element that can be readily added to the element library of an available standard FE package is straightforward. For an element with an internal discontinuity, an augmented physical element with double nodes, i.e., a physical node and a ghost node at each corner as shown in Figs. 3 and 4, can be defined. For example, the physically discontinuous element (1-2-3-4) can be defined as an augmented element 1-2-3-4-1'-2'-3'-4', with the first four nodes as physical nodes and next four ghost nodes. Within the augmented element two properly defined

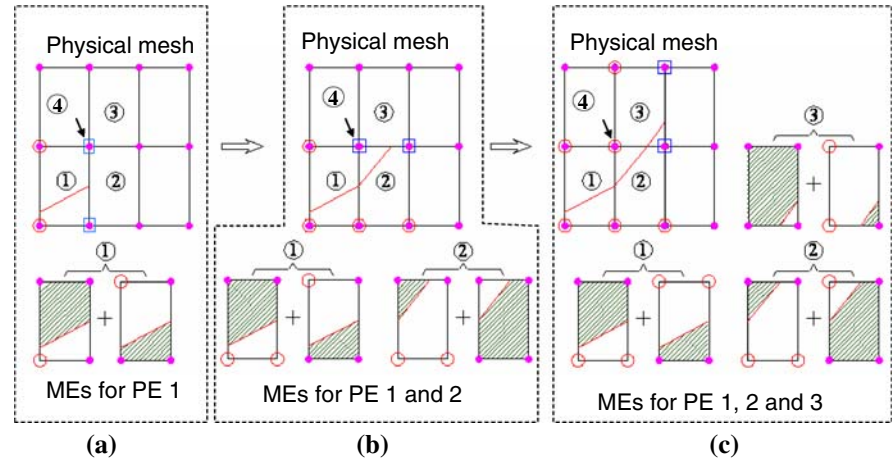
mathematical elements are used to facilitate the calculation of stiffness matrix and nodal forces according to (Eqs. 14–16). The MEs are coupled through the cohesive tractions (Eqs. 7 and 21).

In practice, one can start from a FE mesh with standard FE elements defined by physical nodes only. If an element is continuous (i.e., no internal discontinuity), standard FE procedure can be used to calculate the elemental stiffness and nodal force. Once an existing internal discontinuity is detected, or, by certain criterion, a discontinuity needs to be initiated in the element, ghost nodes are added and the element is replaced by an augmented element with double nodes. In this way, all the neighboring continuous elements are connected to the augmented element through physical nodes, which guarantees displacement continuity across the elemental boundaries. Only those neighboring elements traversed by the discontinuity, which are also augmented, will share both physical and ghost nodes with the augmented element.

Although a ghost node is assigned to each of the physical nodes within the augmented element, situations may rise where some of the ghost nodes may need to remain inactive in either of the mathematical elements due to inter-element continuity requirements. In such cases, the ghost nodes are de-activated by attaching them to the corresponding physical nodes, i.e., enforcing them to have the same displacements as the physical nodes. A simple yet adequate rule to identify these inactive ghost nodes is that any ghost nodes associated with an elemental boundary at which a discontinuity tip resides shall be de-activated.

Such an example is illustrated in Fig. 5. In this case, the discontinuity first enters physical element ① and its tip resides at the right side boundary of this element (Fig. 5a). Then the ghost nodes of two corners at the left side boundary are active (such corners marked as ⊙). At the two corners of the right side boundary where the

Fig. 5 Illustration of the element augmentation process as a discontinuity grows



discontinuity tip resides, the ghost nodes are de-activated (marked as \blacksquare). This is required by the continuity of element ② that shares the same element boundary with element ①. The definitions of the two MEs associated with the augmented physical element ① are illustrated by the two bottom figures, where shaded areas indicate the active material domains in the MEs. As the discontinuity extends to element ② and now its tip resides at the top boundary of this element (Fig. 5b), the ghost nodes at the two corners of bottom boundary of element ② become active. Note that the bottom left corner of this element is shared by element ①. At the top two corners the ghost nodes are de-activated so that the displacements are continuous along this edge as required by element ③. The same procedure repeats as the discontinuity enters element ③. The corresponding MEs within each of the augmented elements at each step are shown in the figures below the physical mesh.

It is interesting to note that the ghost node marked by the arrow becomes active only after elements ①, ②, and ③ are fully traversed by the discontinuity. This is similar to the requirement in X-FEM that a node is enriched only after its support has been completely cut (Moes and Belytschko 2002; Remmers 2006). Our procedure achieves the same purpose but it allows us to work solely on the elemental level. Furthermore, the present procedure does not require the information of whether a physical domain is “below” or “above” a discontinuity, which is a nontrivial issue required in X-FEM.

In 2D fracture problems, wherein a crack is a line entity, the only global information the current formulation requires is the current crack tip position, which can

be stored and updated in a common block accessible to all elements. A sophisticated global tracking algorithm such as the level-set information typically employed in X-FEM is not necessary (although one may choose to set one up for post-processing purposes). Since in the A-FEM formulation, a crack tip always resides on one of the edges of an uncracked element (unless it has reached a boundary), a check is performed before each element stiffness calculation first to see whether the element is hosting a crack-tip (i.e., whether the crack tip coordinates lie in between any two corner nodes of the element) and if so, whether the crack is ready to propagate through it, in which case the element needs to be augmented. The propagation condition is determined by the averaged stress (or strain) in this element, as discussed in more detail in Sect. 5.2. If the crack propagation condition is met, the propagation direction is determined and the crack tip is extended to another edge of the newly cracked element and cohesive tractions are induced along the new fracture surface. With this scheme, the global continuity of the crack is ensured with minimal global tracking efforts.

The above procedure is very convenient to implement in a code for which the source code is available for modification and ghost nodes can therefore be added just to those elements where it is necessary during a calculation. If, however, implementation is in a commercial code where the source code is inaccessible, then a different strategy is required. In this case, all elements where cracks might possibly arise have to be defined prior to the calculation to possess double nodes, using the user element feature. The crack-tip position can be stored and constantly updated in a common block that

is accessible to all user elements. An elemental state variable can be utilized to track the status of the element: if the element is away from a crack, only one set of the nodes (physical nodes) are invoked when the user element is called and the other set of nodes are inactive, making it a regular element; if the element is influenced by a crack, another set of nodes (ghost nodes) are then activated to describe the discontinuity. The rest of the procedure follows the description given above.

The price of this strategy for commercial codes is that the DoFs of the problem will be roughly doubled. However, since most of the ghost nodes away from a crack remain inactive, numerical tests show that doubling the DoFs will lead to a mild 60% increase of CPU time (for a problem of 100,000 DoFs).

4 Elements of a multi-scale model of continuous fiber composites

In the following, we demonstrate the power of the A-FEM in treating hierarchical heterogeneous materials, using the cases of laminated and woven textile composites as study problems. Textile composites, in particular, are one of the most morphologically complex classes of material, containing fiber tows with varying sectional shapes that are interlaced in generally non-periodic patterns and inter-tow matrix volumes of complex shape (e.g., Ko 1989; Cox and Flanagan 1997; Pastore et al. 1993). Experiments show that significant failure events involve mechanisms whose spatial extent is similar to the tow width and therefore cannot be predicted without treating the discrete nature of the tows (Cox et al. 1994, 1996; Pastore et al. 1993). In both laminated and textile composites, failure also involves mechanisms acting at the scale of single fibers, including fiber rupture and fiber-matrix debonding, implying that a high-fidelity predictive model will ultimately be a multi-scale formulation.

The examples cover scales ranging from that of a single fiber (1–10 μm) to that of a fiber tow (0.1–1 mm) and are representative elements of an eventual multi-scale model, in which the solutions at different scales would be formally linked in a computation. In two of the examples, analytical solutions provide validation of the accuracy of the A-FEM.

The A-FEM was implemented in the open-source finite element code FEAP (Zienkiewicz and Taylor 2005).

4.1 Axisymmetric tension acting on a fiber-matrix interface

Figure 6a shows a typical fiber/matrix unit cell under axisymmetric, displacement controlled loading. The outer radius is $b = 10 \times 10^{-6} \text{ m}$ and the embedded fiber radius is $a = 5 \times 10^{-6} \text{ m}$. The modulus and Poisson's ratio for the fiber and matrix are $E_f = 300 \text{ GPa}$; $\nu_f = 0.33$; $E_m = 4 \text{ GPa}$; $\nu_m = 0.4$. The fiber-matrix interface was modeled using the cohesive model introduced in Sect. 2. The cohesive parameters are: $\hat{\sigma} = \hat{\tau} = 100 \text{ MPa}$; $w_{nc} = w_{sc} = 0.1 \times 10^{-6} \text{ m}$; $w_{n1} = w_{s1} = 0.001 \times 10^{-6} \text{ m}$; $w_{n2} = w_{s2} = 0.02 \times 10^{-6} \text{ m}$.

The fracture toughnesses for mode I and mode II are $\Gamma_I = \Gamma_{II} = 5.95 \text{ J/m}^2$. For this simple problem, an exact solution has been derived to evaluate the accuracy and convergence of the numerical solution. The exact solution is

$$p = \begin{cases} k_1 u & 0 \leq u < u_1 \\ k_2 u + \lambda_2 \hat{\sigma} & u_1 \leq u < u_2 \\ k_3 u + \lambda_3 (\hat{\sigma} - K_2^C w_{n2}) & u_2 \leq u < u_3 \\ k_4 u & u \geq u_3 \end{cases} \quad (22)$$

where p is the traction resulting from the applied radial displacement at the outer surface, k_1, k_2, k_3 , and k_4 are the four distinct stiffnesses of the $p - u$ curve, resulting from the interaction of fiber/matrix elasticity and the cohesive interface stiffness; and u_1, u_2 , and u_3 are characteristic displacements at which abrupt changes of stiffness in the $p - u$ curve occur (mainly due to the sudden change of tangential stiffness in the cohesive laws, Fig. 2). A detailed derivation of these constants and characteristic displacements as functions of fiber, matrix and cohesive properties are included in Appendix A.

The analytical solution is plotted in Fig. 7a by the solid line. Four distinct deformation stages characterized by four different slopes are apparent in the $p - u$ curve. The first stage reflects the elastic deformation stage when the interface stress is below the peak cohesive strength. Towards the end of stage one, the cohesive strength of the interface is reached and the interface tangential stiffness becomes zero. As a result the slope becomes near zero (the slightly positive slope is due to the fact that the radial deformation leads to circumferential expansion). When the displacement jump reaches and passes w_{n2} in the cohesive law, the interface cohesive stress decreases linearly with further displacement increase and the interface tangential stiffness

Fig. 6 A typical fiber/matrix unit cell under axial-symmetrical loading (a); and a the numerical model with symmetrical boundary conditions (b)

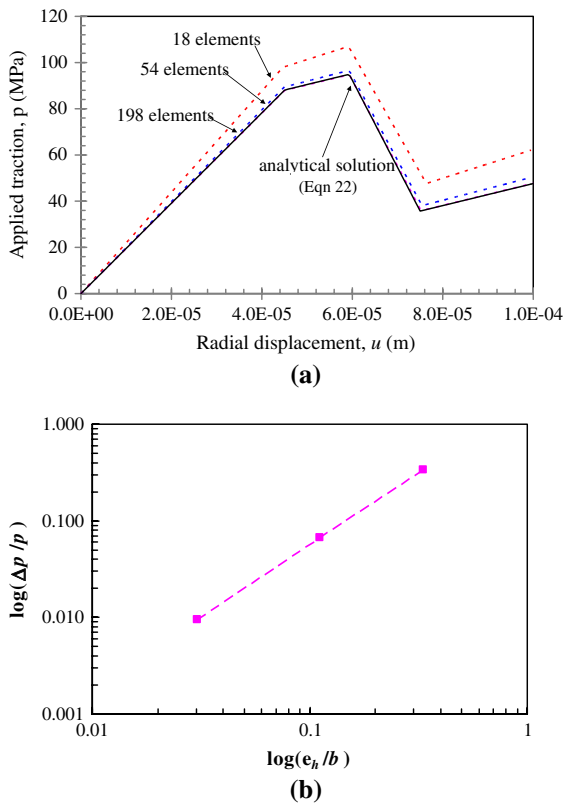
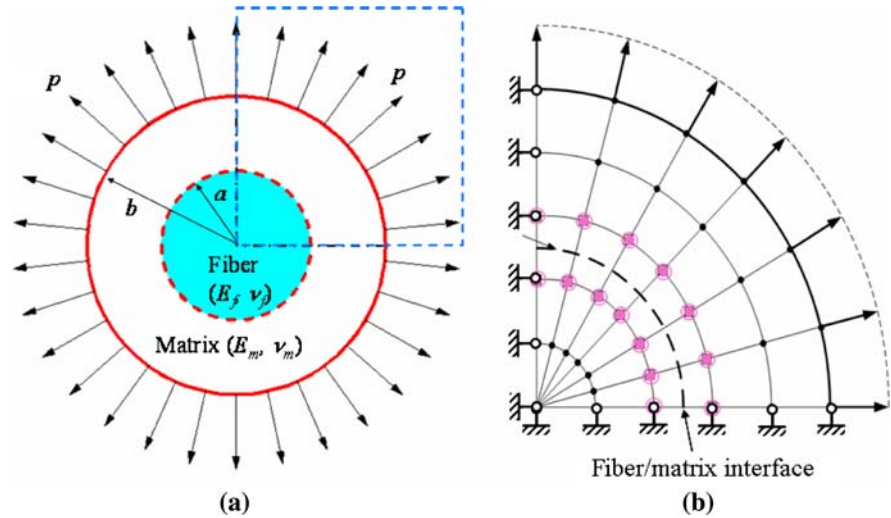


Fig. 7 a Numerically obtained traction–displacement curves with three mesh resolutions as compared to the analytical solution. b Convergence plot showing the rapidly improved accuracy with mesh refinement

becomes negative. This leads to a sharp decrease of p in stage 3. Towards the end of this stage, the critical displacement of the cohesive law is reached and the

matrix is completely separated from the fiber. Therefore, in stage 4 the slope is completely determined by the matrix stiffness.

In numerical modeling, we chose to model a quarter of the domain with symmetrical conditions as shown in Fig. 6b, which also shows one of the meshes used in this study. In order to test the proposed element, the fiber–matrix interface (dashed line) was deliberately set to bisect the elements rather than along element boundaries. Since for this particular problem the location of discontinuity is known a priori, we simply define those elements traversed by the interface as augmented elements with double nodes. These elements are identified in Fig. 6b by encircling of their square nodes. Note that in each of the augmented elements the two domains traversed by the material boundary have very different material properties.

The rest are all traditional 4-node bi-linear elements. This set-up also tests the compatibility of the augmented elements with available traditional elements.

The numerically obtained $p - u$ curves using different mesh resolutions are plotted on Fig. 7a to compare with the analytical solution. All the numerical curves followed the analytically predictions faithfully, and as the mesh resolution increases the numerical results approached the exact solution rapidly. Figure 7b gives the convergence plot showing the normalized numerical error ($|\Delta p|/p_{\text{exact}}$) as a function of normalized characteristic elemental size (e_h/b), where $|\Delta p| = \sqrt{\sum_{i=1}^M (p_i - p_{\text{exact}})^2 / M}$ with p_i being the computed tractions at displacement u_i and e_h is the

elemental size along the radial direction. It is shown in Fig. 7b that the convergence rate is less than the optimal L_2 convergence rate but somewhere between the first and second order of convergence. This is expected because the cohesive law used in this study involves three distinct interface stiffnesses including a negative one. Hansbo and Hansbo (2004) showed that optimal L_2 convergence can be achieved if monotonic, positive stiffness is used.

4.2 Crack propagation in a double cantilever beam (DCB)

To demonstrate the ability of the A-FEM to model long propagating cracks, which is one mode of failure in textile composites, especially in those comprising stacked two-dimensional fabrics, we examine the standard case of a propagating crack in a double cantilever beam (DCB). The DCB is 200 mm long and the beam height is $h = 11$ mm. This is a typical mode-I fracture geometry. The cohesive parameters for fracture are $\hat{\sigma} = 200$ MPa; $w_{nc} = 1.0 \times 10^{-5}$ m; $w_{n1} = 0.0$ m; and $w_{n2} = 2.0 \times 10^{-6}$ m, which result in a mode I toughness of $\Gamma_I = 1200$ J/m². Plane stress conditions were imposed. For simplicity (and more representative of a ceramic composite than a polymer composite), the beam is made of an isotropic elastic material with properties $E = 207$ GPa and $\nu = 0.3$.

The analytical solution chosen for comparison, Eq. 23, is based on classical beam bending theory with transverse shear correction (modified DCB, Cavalli and Thouless 2001). Note that the transverse shear correction term, $[1 + 0.677h/a]^{-1}$, is not rigorous but a semi-empirical one. The analytical fracture load (per unit beam depth) as a function of crack length is shown in Fig. 8.

$$\frac{F}{\Gamma_I} = \sqrt{\frac{1}{12} \frac{Eh}{\Gamma_I}} \left(\frac{a}{h}\right)^{-1} \left[1 + 0.677 \frac{h}{a}\right]^{-1} \quad (23)$$

In the numerical model, no pre-crack was assumed and displacement control of loading was applied as shown in Fig. 8a. The DCB was discretized into 11 layers of elements through the thickness direction and 100 elements per layer along the longitudinal direction. The problem is initially elastic everywhere until a cohesive zone is initiated based on a crack initiation criterion. Robust and efficient criteria for cohesive zone

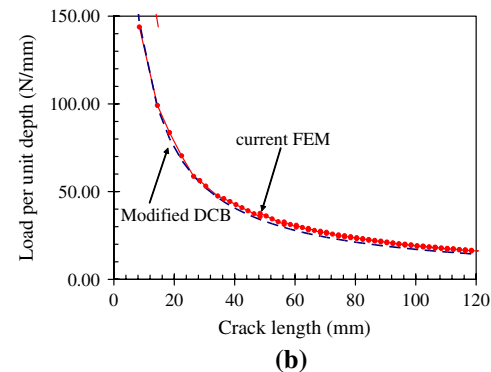
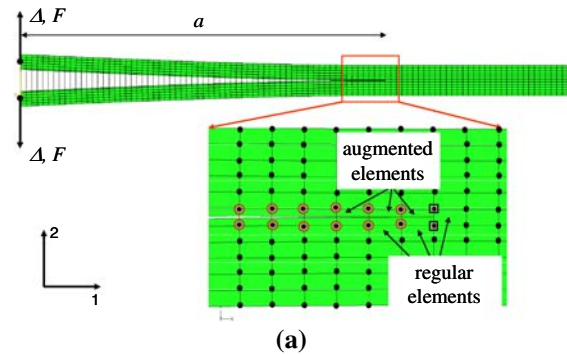


Fig. 8 **a** A deformed DCB with a propagating crack and a magnified view at the current crack-tip showing the augmented elements and neighboring continuous elements and **b** numerically predicted fracture load versus crack length curve compared to an analytical solution (modified DCB)

initiation remain a subject of active research. Historically, such criteria always include a non-local integration domain around the crack tip to obtain a stress-based or energy-based physical quantity, such as the domain averaged maximum principal stress in Wells and Sluys (2001) and the critical stress intensity factor in Moes and Belytschko (2002). In this paper, an element-based criterion is used that refers to the stress or strain state averaged over an entire element, rather than field quantities that are centered on a point.

As will be discussed further in Sect. 5, one of the benefits of employing a cohesive zone for fracture modeling is that the stress field around the tip of a cohesive zone (referred to as the mathematical tip in Moes and Belytschko (2002)) becomes non-singular, i.e., the stress is continuous from the cohesive zone to the undamaged, elastic material immediately ahead of the cohesive zone tip. This suggests the feasibility of using a local, element-based criterion for crack initiation

and propagation. Accordingly, the activation of a cohesive zone and the potential cracking path are determined by the criterion $\bar{\sigma}_{22} = \hat{\sigma}$, where $\bar{\sigma}_{22}$ is the averaged opening stress in an element. The crack growth direction is perpendicular to $\bar{\sigma}_{22}$. Thus, at lower load levels the entire model is elastic until the maximum opening stress ($\bar{\sigma}_{22}$) at the left edge reaches the cohesive strength of $\hat{\sigma}$. (Crack nucleation in elements containing the loading points was suppressed to prevent unphysical crack initiation due to local numerical stress concentration caused by the point loading.)

Since an element remains elastic (cohesive model inactive) until the cohesive crack initiation criterion is satisfied, the large initial stiffness in the cohesive law shown in Fig. 2 is no longer necessary. This large initial stiffness is introduced in traditional cohesive models, where the cohesive elements are planted between solid finite elements along anticipated crack paths and are active from the outset, mainly for numerical stability. However, the large initial stiffness can also lead to spurious deformation modes ahead of a cohesive crack-tip, as noted by [Elises et al. \(2002\)](#), [Yang and Cox \(2005\)](#) and [Remmers \(2006\)](#). By eliminating the initial slope, the cohesive description of the fracture problem is more physically consistent, which can be regarded as another advantage of the current method.

As expected, the numerical model predicts a straight crack along the center line of the beam as evidenced in Fig. 8a. (The straightness of the crack path is a result of the simulation, not a prescription.) The numerically obtained fracture load versus crack length ($F-a$) curve is shown in Fig. 8b by the dotted line; it agrees very well with the analytical solutions (dashed line).

The simple crack extension simulation demonstrates that the A-FEM treats discontinuities locally in the sense that only those elements cut by the crack undergo augmentation. Neighboring continuous elements, even though directly connected to the augmented elements (through physical nodes), are completely unaffected by the augmentation process. This can be seen from the global deformation of the DCB and the magnified view of the current crack-tip region in Fig. 8a. In the magnified crack-tip region, elemental corners marked by solid dots indicate corners at which only physical nodes exist, while encircled solid dots represent corners at which both physical and ghost nodes are active. Two dots enclosed by squares indicate corners where ghost nodes are assigned but are de-activated because the crack tip resides at the boundary connecting the two

corners. Only those elements traversed by the growing crack are augmented, the rest remaining regular standard finite elements.

4.3 Uni-axial tension of a plane-weave textile composite

In this section, we shall demonstrate the potential power of the proposed method in dealing with discontinuities related to geometrically complex material heterogeneity. In many heterogeneous material systems such as particulate reinforced composites and textile composites, generating a coherent standard FE mesh that conforms to all material boundaries is a daunting task, if not impossible. However, with the present method, it is possible to choose a physical mesh that is relieved from the necessity of being in one-to-one correspondence with the material boundaries. We can deal with the material heterogeneity within a physical element by a series of mathematical elements. In order to assure that the displacement field is continuous throughout the element in the absence of damage while some components of the strain field are allowed to be discontinuous at the heterogeneity boundary, as required by continuity of stress, the element augmentation also includes elastic cohesive interface tractions at the heterogeneity boundary. These interface tractions are given a high stiffness, so that their influence on displacement continuity is negligible. With such a treatment, the influence of material heterogeneity is automatically accounted for by sub-domain integration with different material properties in each augmented physical element; while stress continuity (and strain discontinuity) across material boundaries are guaranteed by the elastic cohesive interface.

We demonstrate this capability using a simple plane-weave textile composite (2D) as shown in Fig. 9a. Due to the orthogonal orientation of the fiber tows, there are three different material domains: the longitudinal tows (modulus $E_1 = 140$ GPa in the loading direction and volume fraction $V_1 = 50\%$), the transverse tows (modulus $E_2 = 10$ GPa and volume fraction $V_2 = 32\%$), and the intertow matrix (modulus $E_m = 3$ GPa and volume fraction $V_m = 18\%$). Poisson's ratio is 0.3 for all three material domains. The length of the entire domain is 16 mm while the height is 4 mm. The elastic interface stiffness (the initial slope of the cohesive law) is set to a value that ensures that the small cohesive opening

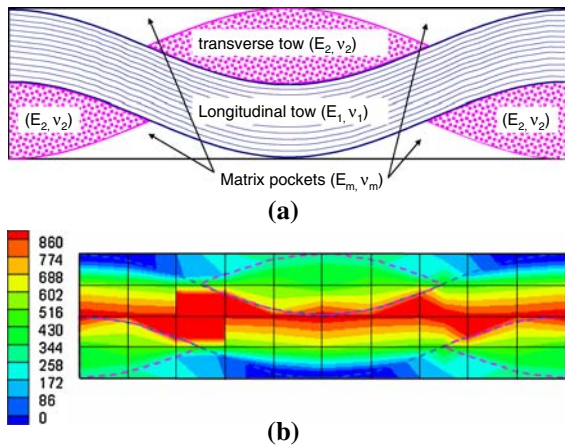


Fig. 9 (a) Material domains in a 2D plane-wave textile composite and (b) contour plot of the A-FEM predicted longitudinal stress (s_{11}) averaged at the nodes of physical elements

across the interface is less than 1% of the deformation of a physical element, had it been entirely filled with the longitudinal tow material.

An analytical estimate of the longitudinal modulus with consideration of the longitudinal tow waviness can be obtained using the method of orientation averaging with waviness (OAWW) proposed by Cox and Dadkhah (1995). The estimated modulus using OAWW for this particular case is 45.6 GPa. This value is within 3% of the FEM result obtained by ABAQUS (46.7 GPa), using a mesh that fully conformed to all the material boundaries.

Even for this highly idealized geometry, creating a coherent FEM mesh that conforms to all the material boundaries is a non-trivial task. However, with the proposed method, the entire domain was simply divided into $10 \times 8 = 80$ cuboidal physical elements (Fig. 9b). A pre-processor was coded to trace each of the material boundaries in such way that, if a physical element was traversed by a material boundary, additional ghost nodes were added to augment the element and the material difference across the boundary was recorded for sub-domain integration. In the case that an element is traversed by two material boundaries, it was augmented twice (so that the discontinuities in the physical element were represented by three MEs). With the elastic cohesive interface used, only weak discontinuities caused by material property mismatch across material boundaries were considered in this calculation.

The modulus predicted by the A-FEM is 46.1 GPa, which is in excellent agreement with the values predicted by OAWW and ABAQUS. The longitudinal stress field calculated by A-FEM is shown in Fig. 9b with both physical elements (solid line) and material boundaries (dashed lines) superimposed. It is obvious from the plot that the stress is continuous across all the material boundaries, which suggests that the A-FEM did a good job of capturing the intra-element stress difference due to material mismatch within augmented elements. Moreover, although a relatively coarse mesh was used, the stress gradient along the thickness direction in the longitudinal tow at locations of tow cross-over was well captured. This local bending in wavy tows due to tow straightening under tension has been recently observed experimentally in textile composites and is responsible for significant composite stiffness reduction due to tow waviness (Yang et al. 2005).

5 Discussions

5.1 Notes on the A-FEM formulation

Lying at the heart of the method proposed in this study is the use of two separable mathematical elements (MEs) to represent a physical element (PE) with an internal strong or weak discontinuity. In Sect. 3, through a simple 4-node element, we have proved that by simply doubling the element corner nodes (a physical node and a ghost node), an arbitrary discontinuity in a PE can be fully described by invoking MEs that are separable from each other. Since each ME (which is a standard FEM element) can represent the physical responses of a corresponding domain in a PE that is severed by a discontinuity, the separation of the two MEs leads to separate approximations of the discontinuous physical domains in a PE. The two MEs are coupled through a cohesive zone model (CZM). Further, the jump in displacements across the discontinuity can be obtained directly from standard nodal interpolation of the two MEs. This greatly facilitates the integration of discontinuities with a wide spectrum of properties, including rigid interfaces, cohesive zone-governed fractures, and complete traction-free separations.

A very similar procedure was proposed by Hansbo and Hansbo (2002, 2004), who elucidated their technique through a 3-node linear element and demonstrated its effectiveness through elliptic interface

problems with *constant* interfacial compliance. The method was further extended by Steinmann and colleagues to incorporate CZMs for arbitrary fracture problems (Jager et al. 2008; Mergheim et al. 2007, 2005). Hansbo and Hansbo's formulation (unfitted FEM) is based on an extension of Nitsche's method, while we have established in Sect. 3.1 that this can alternatively be achieved through simple mapping between MEs and PEs. Further, the current formulation enables us to re-cast the dual-element scheme into a single augmented physical element, which is the key to achieving full compatibility with existing finite element programs.

The current method and Hansbo and Hansbo's method can be regarded as an elemental-based local enrichment method, in distinction to the X-FEM approach of nodal-based enrichment. The most attractive feature of the proposed method is that the augmented element with discontinuity fully preserves elemental locality, an essential advantage of the traditional finite element method. This can be clearly seen from the discussion in Sect. 4.3 and the numerical examples in Sect. 4. Compared to standard FEM, the current method does need to dynamically add in ghost nodes for defining the augmented element. In particular, when dealing with moving discontinuities, the dimension of the problem will increase as a discontinuity traverses more and more elements, because an increasing number of ghost nodes will be added to the problem. Fortunately, as we have demonstrated, ghost nodes are used only by the augmented discontinuous elements and are not shared by the regular, continuous finite elements that are connected to the augmented physical elements. Therefore, an augmented element remains local although its dimension is increased by a factor of two.

As has already been discussed and demonstrated, the method proposed in this study can effectively address a wide variety of stationary or moving discontinuities. X-FEM can achieve the same purpose (Moes et al. 1999; Gravouil et al. 2002; Moes et al. 2002; Moes and Belytschko 2002; Wells et al. 2002; De Borst 2003; Moes et al. 2002; Remmers 2006), but does so by introducing characteristic basis functions or enrichment functions. Our formulation enables us to account for a strong or weak discontinuity within an augmented element using standard nodal shape functions only. There is no need to introduce local enrichment functions as X-FEM does. In the X-FEM formulation, the displace-

ments due to element straining (continuous displacements) and those due to the displacement jump across an internal discontinuity are separately assigned to different nodal DoFs. In our formulation, the nodal displacements of all the physical nodes are total displacements, i.e., they include contributions from the continuous straining of the element, as well as the displacement jump across the discontinuity. Therefore, there will be no ambiguity in connecting the augmented element to other standard FEs.

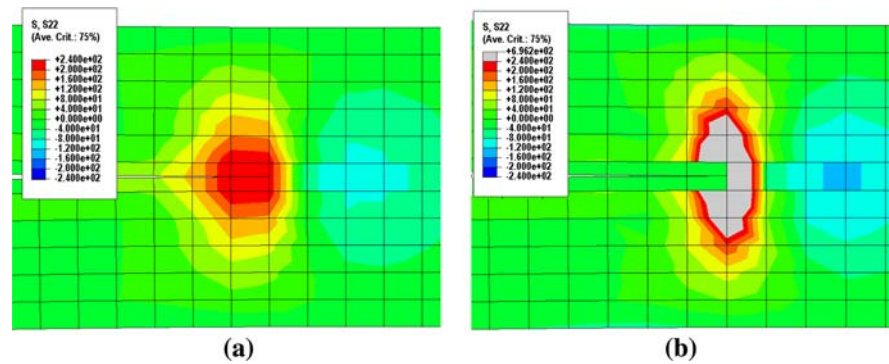
Areias and Belytschko (2006) recently proved that the basis functions of X-FEM and Hansbo and Hansbo's are equivalent. Given the fact that our formulation is similar in spirit with Hansbo and Hansbo (2002, 2004), the same conclusion applies to the current method. However, as noted by Areias and Belytschko (2006) the current formulation makes it much easier to treat nodal DoFs that are not additive such as directors in shell analysis, but is less capable of handling partially cracked elements due to the fact that the crack-tip singularity is not included.

5.2 Choosing the right formulation for brittle and ductile fracture processes

The question of whether to prefer the current formulation or the X-FEM formulation for a particular fracture problem can be referred to the physics of the fracture process. For brittle fracture (with the archetype of glass), where the material presents singular or nearly singular crack tip fields, the nodal enrichment scheme of X-FEM is the more appropriate. In its current formulation, the method presented here cannot account for discontinuities with a singular tip *without breaking the elemental locality*. X-FEM treats the singular fields effectively by introducing the asymptotic solutions as basis functions (Moes et al. 1999). On the other hand, if the fracture process involves a relatively long non-linear process zone, the tip fields are not singular but in fact are relatively uniform near the crack tip, both in the process zone and in the undamaged material ahead of the crack tip. Figure 10a shows the opening stress field (σ_{22}) around the cohesive crack-tip in the DCB studied above (Fig. 8).

It is clearly seen that the σ_{22} is approximately uniform across the cracked element and the adjacent regular (undamaged material) element. In this example, the active cohesive zone covers roughly 3 elements

Fig. 10 (a) Contour plot of opening stress (σ_{22}) around the cohesive crack-tip in the DCB of Fig. 8 and (b) the contour plot of the same DCB under identical remote load but with a traction-free crack (zero cohesive strength). Both were computed using the A-FEM. The highly concentrated crack-tip stress is obvious in (b) but the stress in (a) is fairly continuous



(6 mm), which is in good agreement with the analytical estimate of 6.7 mm provided by nonlinear fracture theory (Yang and Cox 2005). Additional calculations show that this cohesive zone is fairly insensitive to mesh size, as long as the element size is smaller than the cohesive zone length. When this condition is satisfied, the fact that in the present formulation the discontinuity has to move from one element boundary to another, i.e., the tip cannot reside within an element, is physically unimportant because, in the presence of the cohesive zone, the stress is nearly uniform from the cohesive zone to the uncracked material ahead of the crack tip and altering the position of the crack tip within an element cannot affect the stress field in that element very strongly. Therefore (1) a criterion for crack advance that is based on the average stress (or strain) in the uncracked element immediately ahead of a cohesive crack tip is justified; and (2) changes in the global stress fields associated with crack advance will be accurately represented by a model in which the crack tip jumps from one element boundary to the next. Appealingly, the same gauge-averaged criterion serves with equal physical justification for crack initiation in a pristine region of the material.

If the present formulation is employed for a brittle fracture problem, a large stress concentration is predicted (Fig. 10b) in approximation to the ideal singular stress field. However, this result will be strongly mesh-dependent.

5.3 Modeling multiple discontinuities via recursive augmentation

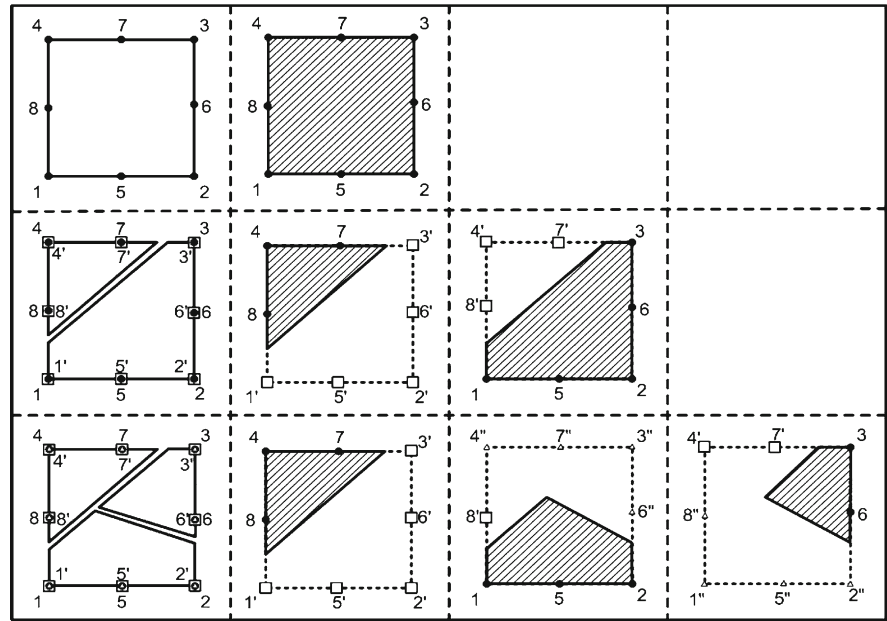
The presented method also offers potentially powerful means to account for multiple discontinuities (e.g., multiple material boundaries or crack branching/

merging) within a physical element, as demonstrated by the numerical example in Sect. 4.3. We further note that the two MEs introduced above can be viewed as two daughter elements of the original physical element, each possessing only part of the active material domain. If one of the daughter elements is further traversed by another discontinuity, the element can then be divided into two new MEs (grand-daughter elements) by adding a new set of ghost nodes. The process can be repeated as necessary in dealing with multiple intra-element discontinuities. This is illustrated in Fig. 11. In this case, the branching cracks can be fully described by three MEs. No matter how many times a physical element is augmented, the displacements of the (original) physical nodes remain total and the physical element can be connected directly to other standard finite elements through the physical nodes. We are developing such a general purpose element package based on an open-source finite element package and will report results elsewhere.

6 Conclusions

In this article, an augmented finite element method (A-FEM) that can fully account for arbitrary intra-elemental discontinuities has been proposed. The formulation is very similar to one previously proposed by Hansbo and Hansbo (2004), but the current approach uses separable mathematical elements, which employ standard FE nodal interpolation only, to construct the augmented finite element. Together with the fact that the augmented element preserves the elemental locality, this property assures full compatibility with standard finite element programs. The formulation proposed also greatly facilitates the integration of cohesive zone models for material damage and failure. Because the

Fig. 11 Illustration of the A-FEM in dealing with multiple intra-element discontinuity



cohesive models are not activated until a failure initiation criterion is satisfied locally, stable computations can be obtained without including a regime of initially high stiffness in the model, which has been the source of unphysical results in prior cohesive fracture modeling. Combination of the A-FEM with cohesive models provides the physical flexibility needed to handle a wide spectrum of discontinuities, including rigidly bonded dissimilar materials, localized damage bands, cohesive fracture, and traction-free cracks.

The A-FEM allows accurate modeling of heterogeneous materials and is especially powerful when dealing with morphologically complex heterogeneity. The consistency of meshing methods at different scales and the recursive feature for repetitive sub-dividing of the mesh make the A-FEM an attractive vehicle for multi-scale simulations.

Acknowledgments Work is supported partially by NASA Langley Research Center (Contract No. NNL08AA19C). DSL also appreciates the support from the Chinese NSF (CNSF#5077 8163) and the National Basic Research Program of China (#2007 CB714200). The derivation of the element augmentation method as it is presented in this paper is solely the work of the first two authors and not the third. The authors are grateful to Dr. Ted. Belytschko for bringing to their attention the work of Hansbo and Hansbo and for his very enlightening remarks on the advantages and disadvantages of different numerical approaches to fracture modeling.

Appendix: an analytical solution to a fiber/matrix UC with CZM interface

A.1 Generic solution to an axial-symmetric plane problems

Figure 12 shows a plane axial-symmetrical problem with inner boundary $r = a$ and outer boundary $r = b$. p_a and p_b are tractions on the inner and outer boundary, respectively. The solution to the radial displacement $u_r(r)$ has the following generic form (Barber 2002),

$$u_r(r) = Ar + B/r, \quad (24)$$

where A and B are two constants to be determined by boundary conditions.

With Eq. 1 the strain and stress fields can then be derived as follows,

$$\epsilon_r(r) = A - \frac{B}{r^2}; \quad \epsilon_\theta(r) = A + \frac{B}{r^2}, \quad (25)$$

and,

$$\begin{aligned} \sigma_r(r) &= (D_1 + D_2)A - (D_1 - D_2)\frac{B}{r^2}; \\ \sigma_\theta(r) &= (D_1 + D_2)A + (D_1 - D_2)\frac{B}{r^2} \end{aligned} \quad (26)$$

D_1 and D_2 are material constants, for plane strain problems

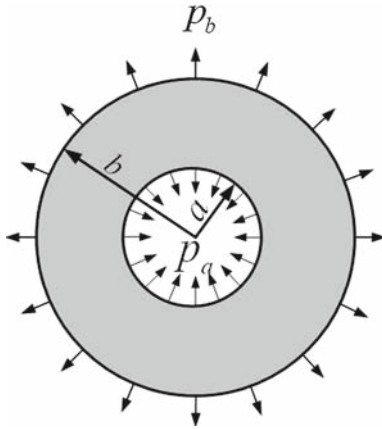


Fig. 12 Geometry and loading of an axisymmetric plane problem

$$\begin{aligned} D_1 &= \frac{1-\nu}{(1+\nu)(1-2\nu)}E; \\ D_2 &= \frac{\nu}{(1+\nu)(1-2\nu)}E, \end{aligned} \quad (27)$$

where E and ν are Young's modulus and Poisson's ratio respectively.

If $a = 0$, B must be zero. From the outer boundary condition $\sigma_r(b) = p_b$, we get

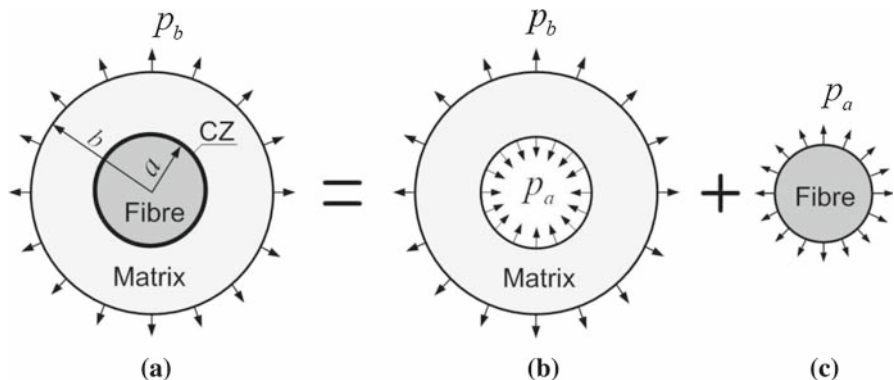
$$p_b = K u_b; \quad (28)$$

where $K = (D_1 + D_2)/b$ and $u_b = u_r(b)$.

If $a \neq 0$, according to the inner and outer boundary conditions $\sigma_r(a) = p_a$ and $\sigma_r(b) = p_b$, we have

$$\begin{aligned} p_a &= -K_{11}u_a + K_{12}u_b \\ p_b &= -K_{21}u_a + K_{22}u_b \end{aligned} \quad (29)$$

Fig. 13 Continuous radial traction across the cohesive interface of the unit cell



where $u_a = u_r(a)$ and K_{ij} ($i = 1, 2; j = 1, 2$) are constants defined below,

$$\begin{aligned} K_{11} &= \frac{a}{b^2 - a^2} \left[(D_1 - D_2) \frac{b^2}{a^2} + (D_1 + D_2) \right]; \\ K_{12} &= \frac{2b}{b^2 - a^2} D_1 \\ K_{22} &= \frac{b}{b^2 - a^2} \left[(D_1 - D_2) \frac{a^2}{b^2} + (D_1 + D_2) \right]; \\ K_{21} &= \frac{2a}{b^2 - a^2} D_1 \end{aligned} \quad (30)$$

A.2 Solution to a fiber/matrix UC with CZM interface

Figure 13 shows a typical fiber/matrix unit cell under axial-symmetric loading. The initial thickness of the interface is assumed to be zero.

Since the radial stress (p_a) is continuous across the cohesive interface, the problem in Fig. 13a can be decomposed into two problems as shown in Fig. 13b, c, which are coupled by the cohesive interface law, $p_a = p_a(w_n)$. Here $w_n = u_a^M - u_a^F$ is the cohesive opening displacement, or displacement jump across the interface. The superscript $(\cdot)^M$ and $(\cdot)^F$ denote matrix and fiber domain, respectively.

From Eq. 28, we can obtain the relation between surface traction, p_a and radial displacement, u_a^F , of the fiber, i.e.,

$$p_a = K^F u_a^F, \quad (31)$$

where $K^F = (D_1^F + D_2^F)/a$.

For the matrix, the tractions at inner and outer surfaces can be expressed by the radial surface displacements using Eq. 29,

$$\begin{aligned} p_a &= -K_{11}^M u_a^M + K_{12}^M u_b^M \\ p_b &= -K_{21}^M u_a^M + K_{22}^M u_b^M \end{aligned} \quad (32)$$

where K_{ij}^M are the K_{ij} in Eq. 30 evaluated with the elastic constants of matrix. u_b^M and p_b are the applied outer surface displacement u and the resulted surface traction p .

The matrix and fiber domains are coupled by the cohesive traction at the interface. According to Eq. 29, the relationship between traction and separation can be rewritten as following

$$p_a = \begin{cases} K_1^C(u_a^M - u_a^F) & \text{if } u_a^M - u_a^F \leq w_{n1} \\ \sigma & \text{if } w_{n1} < u_a^M - u_a^F \leq w_{n2} \\ K_2^C(u_a^M - u_a^F) & \text{if } w_{n2} < u_a^M - u_a^F \leq w_{nc} \\ -K_2^C w_{nc} & \text{if } u_a^M - u_a^F > w_{nc} \\ 0 & \end{cases} \quad (33)$$

Here, $K_1^C = \hat{\sigma}/w_{n1}$ and $K_2^C = -\hat{\sigma}/(w_{nc} - w_{n2})$ are the two stiffnesses associated with interface cohesive law (Fig. 2). Substituting Eq. 33 into 31 to eliminate u_a^F and making use of the first equation of Eq. 32 to eliminate p_a , we can obtain the explicit $p-u$ relation from the second equation of Eq. 32 as below,

$$p = \begin{cases} k_1 u & 0 \leq u < u_1 \\ k_2 u + \lambda_2 \hat{\sigma} & u_1 \leq u < u_2 \\ k_3 u + \lambda_3 (\hat{\sigma} - K_2^C w_{n2}) & u_2 \leq u < u_3 \\ k_4 u & u \geq u_3 \end{cases}, \quad (34)$$

and,

$$\begin{aligned} k_1 &= K_{22}^M - \frac{K_{12}^M K_{21}^M}{K_{11}^M + \frac{K^F K_1^C}{K^F + K_1^C}} \\ k_2 &= K_{22}^M - \frac{K_{12}^M K_{21}^M}{K_{11}^M} \\ k_3 &= K_{22}^M - \frac{K_{12}^M K_{21}^M}{K_{11}^M + \frac{K^F K_2^C}{K^F + K_2^C}} \\ k_4 &= K_{22}^M - \frac{K_{12}^M K_{21}^M}{K_{11}^M} \\ \lambda_2 &= \frac{K_{21}^M}{K_{11}^M} \\ \lambda_3 &= \frac{K^F K_{21}^M}{K_{11}^M (K^F + K_2^C) + K^F K_2^C} \\ u_1 &= \frac{\lambda_2 \hat{\sigma}}{k_1 - k_2} \\ u_2 &= \frac{1}{k_2 - k_3} \left[(\lambda_3 - \lambda_2) \hat{\sigma} - \lambda_3 K_2^C w_{n2} \right] \\ u_3 &= \frac{\lambda_3}{k_4 - k_3} (\hat{\sigma} - K_2^C w_{n2}) \end{aligned}$$

References

- Areias PMA, Belytschko T (2006) A comment on the article: a finite element method for simulation of strong and weak discontinuities in solid mechanics. *Comput Methods Appl Mech Eng* 195:1275–1276. doi:[10.1016/j.cma.2005.03.006](https://doi.org/10.1016/j.cma.2005.03.006)
- Ashby MF (1992) Physical modelling or materials problems. *Mater Sci Technol* 8:102–111
- Barber JR (2002) Elasticity. Kluwer Academic Press, New York
- Belytschko T, Black T (1999) Elastic crack growth in finite elements with minimal remeshing. *Int J Numer Methods Eng* 45:601–620. doi:[10.1002/\(SICI\)1097-0207\(19990620\)45:5<601::AID-NME598>3.0.CO;2-S](https://doi.org/10.1002/(SICI)1097-0207(19990620)45:5<601::AID-NME598>3.0.CO;2-S)
- Belytschko T, Moes N, Usui S, Parimi C (2001) Arbitrary discontinuities in finite elements. *Int J Numer Methods Eng* 50:993–1013. doi:[10.1002/1097-0207\(20010210\)50:4<993::AID-NME164>3.0.CO;2-M](https://doi.org/10.1002/1097-0207(20010210)50:4<993::AID-NME164>3.0.CO;2-M)
- Camanho PP, Dávila CG, et al (2003) Numerical simulation of mixed-mode progressive delamination in composite materials. *J Compos Mater* 37:1415–1438. doi:[10.1177/0021998303034505](https://doi.org/10.1177/0021998303034505)
- Carpinteri A, Ferro G (2003). Fracture assessment in concrete structures. In: Milne I, Ritchie RO, Karihaloo B (eds) *Concrete structure integrity*, vol 7. Elsevier Science, Amsterdam
- Cavalli MN, Thouless MD (2001) The effect of damage nucleation on the toughness of an adhesive joint. *J Adhes* 76:75–92. doi:[10.1080/00218460108029618](https://doi.org/10.1080/00218460108029618)
- Chang KY, Liu S et al (1991) Damage tolerance of laminated composites containing an open hole and subjected to tensile loadings. *J Compos Mater* 25:274–301
- Chessa J, Wang H, et al (2003) On the construction of blending elements for local partitioning of unity enriched finite elements. *Int J Numer Methods Eng* 57:1015–1038. doi:[10.1002/nme.777](https://doi.org/10.1002/nme.777)
- Cox BN, Dadkhah MS (1995) The macroscopic elasticity of 3D woven composites. *J Compos Mater* 29:785–819
- Cox BN, Flanagan G (1997) Handbook of analytical methods for textile composites. NASA Contractor Report 4750, NASA Langley Research Center, Hampton, Virginia
- Cox BN, Yang QD (2006) In quest of virtual tests for structural composites. *Science* 314:1102–1107. doi:[10.1126/science.1131624](https://doi.org/10.1126/science.1131624)
- Cox BN, Dadkhah MS, Inman RV, Morris WL, Zupon J (1992) Mechanisms of compressive failure in 3D composites. *Acta Metall Mater* 40:3285–3298. doi:[10.1016/0956-7151\(92\)90042-D](https://doi.org/10.1016/0956-7151(92)90042-D)
- Cox BN, Dadkhah MS, Morris WL, Flintoff JG (1994) Failure mechanisms of 3D woven composites in tension, compression, and bending. *Acta Metall Mater* 42:3967–3984. doi:[10.1016/0956-7151\(94\)90174-0](https://doi.org/10.1016/0956-7151(94)90174-0)
- Cox BN, Dadkhah MS, Morris WL (1996) On the tensile failure of 3D woven composites. *Compos A* 27:447–458. doi:[10.1016/1359-835X\(95\)00053-5](https://doi.org/10.1016/1359-835X(95)00053-5)
- Cox BN, Spearing SM, Mumm DR (2008). In: PP Camanho, CG Dávila, ST Pinho, JJC Remmers (eds) *Mechanical Response of Composites*. Springer Science and Business Media, Dordrecht, pp. 57–75
- De Borst R (2003) Numerical aspects of cohesive-zone models. *Eng Fract Mech* 70:1743–1752. doi:[10.1016/S0013-7944\(03\)00122-X](https://doi.org/10.1016/S0013-7944(03)00122-X)

- Elices M, Guinea GV, et al (2002) The cohesive zone model: advantages, limitations and challenges. *Eng Fract Mech* 69:137–163. doi:[10.1016/S0013-7944\(01\)00083-2](https://doi.org/10.1016/S0013-7944(01)00083-2)
- Fries TP, Belytschko T (2006) The intrinsic XFEM: a method for arbitrary discontinuities without additional unknowns. *Int J Numer Methods Eng* 68:1358–1385. doi:[10.1002/nme.1761](https://doi.org/10.1002/nme.1761)
- Gonzalez C, Lorca JL (2006) Multiscale modeling of fracture in fiber-reinforced composites. *Acta Mater* 54:4171–4181. doi:[10.1016/j.actamat.2006.05.007](https://doi.org/10.1016/j.actamat.2006.05.007)
- Gravouil A, Moes N, et al (2002) Non-planar 3D crack growth by the extended finite element and level sets—part II: level set update. *Int J Numer Methods Eng* 53:2569–2586. doi:[10.1002/nme.430](https://doi.org/10.1002/nme.430)
- Hallett S, Wisnom MR (2006) Numerical investigation of progressive damage and the effect of layup in notched tensile tests. *J Compos Mater* 40:1229–1245. doi:[10.1177/0021998305057432](https://doi.org/10.1177/0021998305057432)
- Hansbo A, Hansbo P (2002) An unfitted finite element method, based on Nitsche's method, for elliptic interface problems. *Comput Methods Appl Mech Eng* 191:5537–5552. doi:[10.1016/S0045-7825\(02\)00524-8](https://doi.org/10.1016/S0045-7825(02)00524-8)
- Hansbo A, Hansbo P (2004) A finite element method for the simulation of strong and weak discontinuities in solid mechanics. *Comput Methods Appl Mech Eng* 193:3523–3540. doi:[10.1016/j.cma.2003.12.041](https://doi.org/10.1016/j.cma.2003.12.041)
- Iarve EV, Mollenhauer D et al (2005) Theoretical and experimental investigation of stress redistribution in open-hole composite laminates due to damage accumulation. *Compos Part A* 36:163–171
- Jager P, Steinmann P, et al (2008) On local tracking algorithms for the simulation of three-dimensional discontinuities. *Comput Mech* 42:395–406. doi:[10.1007/s00466-008-0249-3](https://doi.org/10.1007/s00466-008-0249-3)
- Karihaloo BL, Xiao QZ (2003) Modeling of stationary and growing cracks in FE framework without remeshing: a state-of-art review. *Comput Struc* 81:119–129. doi:[10.1016/S0045-7949\(02\)00431-5](https://doi.org/10.1016/S0045-7949(02)00431-5)
- Ko FK (1989) Preform architecture for ceramic-matrix composites. *Ceram Bull* 68:401–414
- McCartney LN (2003) Physically based damage models for laminated composites. *J Mater Des Appl* 217:163–199
- Melenk JM, Babuska I (1996) The partition of unity finite element method: basic theory and applications. *Comput Methods Appl Mech Eng* 139:289–314. doi:[10.1016/S0045-7825\(96\)01087-0](https://doi.org/10.1016/S0045-7825(96)01087-0)
- Mergheim J, Huhl E, et al (2005) A finite element method for the computational modeling of cohesive cracks. *Int J Numer Methods Eng* 63:276–289. doi:[10.1002/nme.1286](https://doi.org/10.1002/nme.1286)
- Mergheim J, Huhl E, et al (2007) Towards the algorithmic treatment of 3D strong discontinuities. *Commun Numer Methods Eng* 23:97–108. doi:[10.1002/cnm.885](https://doi.org/10.1002/cnm.885)
- Moes N, Belytschko T (2002) Extended finite element method for cohesive crack growth. *Eng Fract Mech* 69:813–833. doi:[10.1016/S0013-7944\(01\)00128-X](https://doi.org/10.1016/S0013-7944(01)00128-X)
- Moes N, Dolbow J, et al (1999) Finite element method for crack growth without remeshing. *Int J Numer Methods Eng* 46:131–150. doi:[10.1002/\(SICI\)1097-0207\(19990910\)46:1<131::AID-NME726>3.0.CO;2-J](https://doi.org/10.1002/(SICI)1097-0207(19990910)46:1<131::AID-NME726>3.0.CO;2-J)
- Moes N, Gravouil A, et al (2002) Non-planar 3D crack growth by the extended finite element and level sets—part I: mechanical model. *Int J Numer Methods Eng* 53:2549–2568. doi:[10.1002/nme.429](https://doi.org/10.1002/nme.429)
- Pastore CM, Bogdanovich AE, Goward YA (1993) Applications of a meso-volume-based analysis for textile composite structures. *Compos Eng* 3:181–194. doi:[10.1016/0961-9526\(93\)90041-H](https://doi.org/10.1016/0961-9526(93)90041-H)
- Remmers JC (2006) Discontinuities in materials and structures—a unifying computational approach. Ph.D Thesis, Delft University
- Shahwan KW, Waas AM (1997) Non-self-similar decohesion along a finite interface of unilaterally constrained delaminations. *Proc R Soc Lond A* 453:515–555. doi:[10.1098/rspa.1997.0029](https://doi.org/10.1098/rspa.1997.0029)
- Talreja R (2006) Multiscale modeling in damage mechanics of composite materials. *J Mater Sci* 41:6800–6812. doi:[10.1007/s10853-006-0210-9](https://doi.org/10.1007/s10853-006-0210-9)
- Tay TE (2003) Characterization and analysis of delamination fracture in composites: an overview of developments from 1990 to 2001. *Appl Mech Rev* 56:1–32. doi:[10.1115/1.1504848](https://doi.org/10.1115/1.1504848)
- Tvergaard V, Hutchinson JW (1996) On the toughness of ductile adhesive joints. *J Mech Phys Solids* 44:789–800
- Van de Meer FP, Sluys LJ (2008) Continuum models for the analysis of progressive failure in composite laminates. *J Compos Mater* (in press)
- Wang JS, Suo Z (1990) Experimental determination of interfacial toughness using Brazil-nut-sandwich. *Acta Metall* 38:1279–1290. doi:[10.1016/0956-7151\(90\)90200-Z](https://doi.org/10.1016/0956-7151(90)90200-Z)
- Wells GN, Sluys LJ (2001) A new method for modeling cohesive cracks using finite elements. *Int J Numer Methods Eng* 50:2667–2682. doi:[10.1002/nme.143](https://doi.org/10.1002/nme.143)
- Wells GN, De Borst R, et al (2002) A consistent geometrically non-linear approach for delamination. *Int J Numer Methods Eng* 54:1333–1355. doi:[10.1002/nme.462](https://doi.org/10.1002/nme.462)
- Wisnom MR, Chang F-K (2000) Modeling of splitting and delamination in notched cross-ply laminates. *Compos Sci Technol* 60:2849–2856. doi:[10.1016/S0266-3538\(00\)00170-6](https://doi.org/10.1016/S0266-3538(00)00170-6)
- Xie D, Amit G, et al (2006) Discrete cohesive zone model to simulate static fracture in 2D tri-axially braided carbon fiber composites. *J Compos Mater* 40:2025–2046. doi:[10.1177/0021998306061320](https://doi.org/10.1177/0021998306061320)
- Yang QD, Thouless MD (2001) Mixed mode fracture of plastically-deforming adhesive joints. *Int J Fract* 110:175–187. doi:[10.1023/A:1010869706996](https://doi.org/10.1023/A:1010869706996)
- Yang QD, Cox BN (2003) Spatially averaged local strains in textile composites via the binary model formulation. *J Eng Mater Technol* 125:418–425. doi:[10.1115/1.1605117](https://doi.org/10.1115/1.1605117)
- Yang QD, Cox BN (2005) Cohesive zone models for damage evolution in laminated composites. *Int J Fract* 133(2):107–137. doi:[10.1007/s10704-005-4729-6](https://doi.org/10.1007/s10704-005-4729-6)
- Yang QD, Thouless MD, et al (1999) Numerical simulations of adhesively-bonded beams failing with extensive plastic deformation. *J Mech Phys Solids* 47:1337–1353. doi:[10.1016/S0022-5096\(98\)00101-X](https://doi.org/10.1016/S0022-5096(98)00101-X)
- Yang QD, Rugg KL, et al (2005) Evaluation of macroscopic and local strains in a 3D woven C/SiC composite. *J Am Ceram Soc* 88:719–725. doi:[10.1111/j.1551-2916.2005.00156.x](https://doi.org/10.1111/j.1551-2916.2005.00156.x)
- Zienkiewicz OC, Taylor RL (2005) The finite element method. Elsevier, Oxford